

Direct measurement of topological numbers with spins in diamond

Fei Kong,^{1†} Chenyong Ju,^{1,2†} Ying Liu,^{1†} Chao Lei,^{1,2} Mengqi Wang,¹ Xi Kong,^{1,2}
Pengfei Wang,^{1,2} Pu Huang,^{1,2} Zhaokai Li,^{1,2} Fazhan Shi,^{1,2} Liang Jiang,^{3*} Jiangfeng
Du^{1,2*}

¹*National Laboratory for Physical Sciences at the Microscale and Department of Modern Physics, University of Science and Technology of China, Hefei, 230026, China*

²*Synergetic Innovation Center of Quantum Information and Quantum Physics, University of Science and Technology of China, Hefei, 230026, China*

³*Department of Applied Physics, Yale University, New Haven, Connecticut 06511, USA*

Topological numbers can characterize the transition between different topological phases, which are not described by Landau's paradigm of symmetry breaking. Since the discovery of quantum Hall effect, more topological phases have been theoretically predicted and experimentally verified. How-

*e-mail: liang.jiang@yale.edu; djf@ustc.edu.cn [†]These authors contributed equally to this work.

ever, it is still an experimental challenge to directly measure the topological number of various predicted topological phases. In this paper, we demonstrate quantum simulation of topological phase transition of a quantum wire (QW) using a single nitrogen-vacancy (NV) center in diamond. Deploying quantum algorithm of finding eigenvalues, we can reliably extract both the dispersion relations and topological numbers.

Topological numbers were first introduced by Dirac to justify the quantization of electric charge ¹, and later developed into a theory of magnetic monopoles as topological defects of a gauge field ². An amazing fact is that fundamental quantized entities may be deduced from a continuum theory ³. Later on, topological numbers were used to characterize the quantum Hall effect ^{4,5} in terms of transition between topological phases ⁶. Since the topological number in quantum Hall systems is directly proportional to the resistance in transport experiment, its robustness against local perturbations enables a practical standard for electrical resistance ⁴. In the past few years, more topological materials have been discovered, including topological insulators^{7,8}, topological superconductor^{9,10}, and etc.

Developing robust techniques to probe topological numbers becomes an active research topic of both fundamental and practical importance. Recently, a

generalized method of extracting topological number by integrating dynamic responses has been proposed ¹¹. Guided by this theoretical proposal, experiments have successfully measured the topological Chern number of different topological phases using superconducting circuits ^{12,13}. However, their measurement of Chern number requires integration over continuous parameter space, which may not give an exactly discretized topological number. Different from the above integration approach, here we take the simulation approach ^{14–16} and use a single NV center in natural diamond at room temperature ^{17,18} to simulate a topological system. Moreover, we deploy quantum algorithm of finding eigenvalues to map out the dispersion relations ^{19,20} and directly extract the topological number, which enables direct observation of the simulated topological phase transition.

We consider the topological phase transition associated with a semiconductor quantum wire with spin-orbital interaction, coupled to s-wave superconductor and magnetic field ^{9,21–23}. At the boundary between different topological phases of the quantum wire, Majorana bound states can be created as a promising candidate for topological quantum information processing ²⁴. The Hamiltonian of this system can be described using Nambu spinor basis $\psi^T = (\psi_\uparrow, \psi_\downarrow, \psi_\downarrow^\dagger, -\psi_\uparrow^\dagger)$:

$$H_{\text{QW}} = p\sigma_z\tau_z + (p^2 - \mu)\tau_z + \Delta\tau_x + B_x\sigma_x, \quad (1)$$

with the momentum p , chemical potential μ , pairing amplitude Δ , Zeeman energy B_x , and Pauli matrices σ_a and τ_a acting in the spin and particle-hole sectors respectively. Without loss of generality, we may assume negative μ , non-negative B_x and Δ .

The system described by equation (1) has two different topological phases determined by the relative strength of $\{B_x, \mu, \Delta\}$: (i) the trivial superconductivity phase (denoted by SC phase) when $B_x < \sqrt{\Delta^2 + \mu^2}$, and (ii) the topological superconductivity phase (denoted as TP phase) when $B_x > \sqrt{\Delta^2 + \mu^2}$. The phase diagram and dispersion relations of different phases are illustrated in Fig. 1a. There are four energy bands for this system, consisting of two particle bands and two hole bands. We may label the energy bands as 1, 2, 3, 4 from bottom to up as in Fig. 1a. The gap between the 2nd and 3rd bands will disappear during the phase transition. To illustrate the distinct topological nature associated with the SC and TP phases, we may consider the transformed Hamiltonian $\tilde{H}_{QW} = U_p H_{QW} U_p^\dagger$ with unitary transformation $U_p = \exp[i\theta_p \cdot \tau_y]$ and $\theta = \frac{1}{2} \arctan \frac{\Delta}{p^2 - \mu}$, which preserve eigenenergies and all energy bands. Then, we plot the normalized Bloch vector of the reduced eigenstate of the 3rd band in the Bloch sphere associated with the particle-hole sector (i.e., taking a partial-trace over the spin sector for the

3rd eigenstate). As shown in Fig. 1b, when the momentum p changes from 0 to ∞ , the trajectory of the state vector for the SC phase forms a closed loop, while for the TP phase it remains an open trajectory starting from one pole and ending at the opposite pole. Here we treat $p \rightarrow -\infty$ and $p \rightarrow +\infty$ as identical to one another, as $H_{\text{QW}} \rightarrow p^2 \tau_z$ for the both cases. This implies an inversion of the particle and hole bands for the TP phase (but not for the SC phase) with increasing momentum from $p = 0$ to $p \rightarrow \infty$. The two types of topologically different trajectories imply the existence of distinct topological phases for the system. Mathematically, a topological number can be introduced to distinguish these two phases:

$$\nu \equiv \text{sgn}[\text{Pf}(H_{\text{QW}}(p = 0))] \cdot \text{sgn}[\text{Pf}(H_{\text{QW}}(p \rightarrow \infty))], \quad (2)$$

where Pf is the Pfaffian²⁵ with $\text{Pf}(H_{\text{QW}}(p)) = \text{Pf}(\tilde{H}_{\text{QW}}(p))$ for $U_p^\dagger = U_p^T$. Specifically, $\text{Pf}(H_{\text{QW}}(p = 0)) = -B_x^2 + \mu^2 + \delta^2$ and $\text{Pf}(H_{\text{QW}}(p \rightarrow \infty)) = p^4$, the value of ν is determined by the sign of the quantity $-B_x + \sqrt{\mu^2 + \Delta^2}$, which is one of eigenenergies of $H_{\text{QW}}(p = 0)$. The corresponding eigenstate can be represented by $|\Phi\rangle = |\Phi_\sigma\rangle \otimes |\Phi_\tau\rangle$, where $|\Phi_\sigma\rangle$ and $|\Phi_\tau\rangle$ are the eigenstates of $B_x \sigma_x$ and $-\mu \tau_z + \Delta \tau_x$ with eigenenergies $-B_x$ and $\sqrt{\mu^2 + \Delta^2}$ respectively. It is direct to deduce $|\Phi_\sigma\rangle = |\leftarrow\rangle = (|\uparrow\rangle - |\downarrow\rangle)/\sqrt{2}$ ($|\uparrow\rangle$ and $|\downarrow\rangle$ means spin up and down) and $|\Phi_\tau\rangle = \alpha |p\rangle + \beta |h\rangle$ ($|p\rangle$ and $|h\rangle$ means particle and hole) which is dominated by $|p\rangle$ (i.e. $|\alpha|^2 > |\beta|^2$). Therefore, we can apply quantum algo-

rithm of finding eigenvalues²⁰ for the state $|\Phi\rangle$ to directly obtain the eigenenergy $-B_x + \sqrt{\mu^2 + \Delta^2}$, the sign of which is exactly the topological number ν .

The QW Hamiltonian is simulated by a highly controllable two-qubit solid-state system, which is a color defect named NV center in diamond consisting of a substitutional nitrogen atom and a adjacent vacancy, as shown in Fig. 2a. The electrons around the defect form an effective electron spin with a spin triplet ground state ($S = 1$) and couple with the nearby ^{14}N nuclear spin. With an external magnetic field B_0 along the N-V axis, the Hamiltonian of the NV system is ($\hbar = 1$)²⁶:

$$H_{\text{NV}}^0 = -\gamma_e B_0 S_z - \gamma_n B_0 I_z + D S_z^2 + Q I_z^2 + A S_z I_z, \quad (3)$$

where S_z and I_z are the spin operators of the electron spin (spin-1) and the ^{14}N nuclear spin (spin-1), respectively. The electron and nuclear spins have gyromagnetic ratios $\gamma_e/2\pi = -28.03 \text{ GHz/T}$ and $\gamma_n/2\pi = 3.077 \text{ MHz/T}$, respectively. $D/2\pi = 2.87 \text{ GHz}$ is the axial zero-field splitting parameter for the electron spin, $Q/2\pi = -4.945 \text{ MHz}$ is the quadrupole splitting of the ^{14}N nuclear spin, and $A/2\pi = -2.16 \text{ MHz}$ is the hyperfine coupling constant. There are nine energy levels, $|1\rangle, \dots, |9\rangle$, as labeled in Fig. 2b. The simulation is performed in the subspace spanned by $\{|4\rangle, |5\rangle, |7\rangle, |8\rangle\}$, associated with the electron spin

states $\{m_e = 0, -1\}$ (encoding the pseudospin σ) and the nuclear spin states $\{m_n = 0, 1\}$ (encoding the pseudospin τ). The NV spins are radiated by two microwave (MW) pulses and two radio-frequency (RF) pulses simultaneously, which selectively drive the two electron-spin transitions and the two nuclear-spin transitions respectively (Fig. 2b). While the frequencies of the pulses are all slightly detuned from resonance. The frequency detunings for the two MW (RF) pulses are set to be the same value δ_{MW} (δ_{RF}). In the rotating frame, the Hamiltonian can be written as (see SI for the detail)

$$H_{\text{NV}}^{\text{rot}} = \frac{\Omega_{\text{MW1}} - \Omega_{\text{MW2}}}{4} \sigma_x \tau_z - \frac{1}{2} \delta_{\text{RF}} \tau_z + \frac{\Omega_{\text{MW1}} + \Omega_{\text{MW2}}}{4} \sigma_x + \frac{\Omega_{\text{RF}}}{2} \tau_x - \frac{1}{2} \delta_{\text{MW}} \sigma_z, \quad (4)$$

where $\Omega_{\text{MW1,2}}$ are the Rabi frequencies of the two electron spin transitions, Ω_{RF} is the nuclear spin Rabi frequency that is set to the same value for the two nuclear spin transitions. By choosing $\Omega_{\text{MW1}} = -\Omega_{\text{MW2}} = \Omega_{\text{MW}}$, the parameters for the QW system and the NV spins can be identified as the following: $p \sim \Omega_{\text{MW}}/2$, $p^2 - \mu \sim -\delta_{\text{RF}}/2$, $\Delta \sim \Omega_{\text{RF}}/2$, and $B_x \sim -\delta_{\text{MW}}/2$ ¹. Hence, H_{QW} can be exactly reproduced up to a Hadamard gate on the electron spin transforming the spin operators $\sigma_x \leftrightarrow \sigma_z$ in $H_{\text{NV}}^{\text{rot}}$. The Hadamard gate does not change the eigenvalues

¹when performing the experiment, the numerical values of the left side are reduced by a factor of 11 to be coincide with the typical values of NV parameters

and can be fully compensated by modifying the basis states in the experiment. As shown in Fig. 2c, the four states of the NV system can be mapped to QW system one-to-one.

To obtain the energy-dispersion relations of QW and calculate the topological number, we deploy a quantum algorithm of finding eigenvalues²⁰ to measure the eigenvalues of QW. The initial state of the NV spins is prepared to $(|6\rangle + |\Psi\rangle) / \sqrt{2}$, where $|6\rangle$ is used as a reference state and $|\Psi\rangle = |4\rangle, |5\rangle, |7\rangle$, or $|8\rangle$. In general $|\Psi\rangle$ can be expanded by the QW eigenstates $|\Psi\rangle = \sum_{j=1}^4 c_{\psi,j} |\phi_j\rangle$ ($H_{\text{QW}} |\phi_j\rangle = E_j |\phi_j\rangle$). By applying the simulating pulses for an adjustable period $m\tau$ ($m \in \mathbb{N}$), $|\Psi\rangle$ evolves under the effective QW Hamiltonian and accumulates phases $\propto E_j m\tau$ with the state becoming $(|6\rangle + \sum_{j=1}^4 c_{\psi,j} e^{-i2\pi E_j m\tau} |\phi_j\rangle) / \sqrt{2}$. It can be transformed back into the representation of NV spin states ($|\phi_j\rangle = \sum_{l=4,5,7,8} c_{l,j}^* |l\rangle$) and can be written as $(|6\rangle + \sum_{l=4,5,7,8} a_{l,m} |l\rangle) / \sqrt{2}$, with coefficients $a_{l,m} = \sum_{j=1}^4 c_{\psi,j} c_{l,j}^* e^{-i2\pi E_j m\tau}$ which is a function of the QW eigenvalues. The coefficient of $|\Psi\rangle$, i.e. $a_{\psi,m}$, can be measured in the experiment. Therefore, the energy spectrum of the QW Hamiltonian can be obtained by Fourier transforming of the time-domain signals $\{a_{\psi,m}\}$. There will be at most four peaks in the energy spectrum with their heights $\propto |c_{\psi,j}|^2$. Since the 1st and 4th en-

ergy bonds are trivial, we only care about the 2nd and 3rd energy bonds. As $|c_{5(7),2}|^2 + |c_{5(7),3}|^2 \gg |c_{4(8),2}|^2 + |c_{4(8),3}|^2$ in the case of low momentum $|p| \ll \infty$ (see SI), $|\Psi\rangle$ can be $|5\rangle$ or $|7\rangle$ in the experiment. However, the detection of $\{a_{4,m}\}$ is easier than that of $\{a_{7,m}\}$. By reversing the sign of δ_{MW} and σ_z simultaneously in equation (4), one can see that the Hamiltonian remains unchanged. It means $|\Psi\rangle$ can choose $|4\rangle$ instead of $|7\rangle$ by using $\delta'_{\text{MW}} = -\delta_{\text{MW}}$.

The experimental realization was preformed on a home-build set-up which has been described early ²⁷. The external statistic magnetic field was adjusted around 50 mT in order to polarize the ^{14}N nuclear spin using dynamic polarization technology ²⁸. The experimental process is shown in Fig. 3a. At first, the NV system was prepared to $|4\rangle$ by a 4 μs laser pulse, then transformed to the superposition state $(|6\rangle + |\Psi\rangle)/\sqrt{2}$ during the initialization process. ($|\Psi\rangle = |5\rangle$ by the second row RF pulses and $|\Psi\rangle = |4\rangle$ by the third row RF pulses shown in the brackets). After that, the two RF pulses and the two MW pulses described above were applied simultaneously with time length $m\tau$ in order to simulate the QW Hamiltonian. Finally, the state was rotated back to $|4\rangle$ with phase shift θ and the photoluminescence was detected. As shown in Fig. 3b, increasing the θ would lead to oscillating photoluminescence. $a_{\psi,m}$ could be obtained from the os-

cillation amplitude and phase (see METHOD for the detail). With different pulse length $m\tau$, we observed the time-domain evolution of $a_{\psi,m}$ (see Fig. 3c). The eigenvalue of the simulated Hamiltonian can be acquired by the Fourier transform of this time-domain signal (Fig. 3d).

Fig. 4a shows the energy dispersion relations obtained in experiment for the two SC points ($\mu = -1.6, -1.44$), two TP points ($\mu = -1.14, -0.98$), and the critical point ($\mu = -1.29$), given $\Delta = 0.165$ and $B_x = 1.3$. The experimental results agree well with the theoretical expectations except for the TP points. The small energy gap in TP phase disappears due to the fluctuating magnetic field from the surrounding ^{13}C spin bath, which induces phase errors on the NV electron spin. The phase errors will cause not only peak broadening but also peak shifting on the energy spectrum. In addition, the pulses applied are not perfectly selective pulse, the crosstalk between these pulses will also cause slightly peak shift on the energy spectrum. The red lines in Fig. 4a give the numerical calculated energy dispersion including these imperfections which nicely coincide with the experimental results (detailed analysis in SI). Further numerical simulation suggests that the energy gap can be observed if a NV sample with longer electron spin coherence time is adopted ²⁹.

Even though the small energy gap of the TP phase is difficult to resolve at the current experimental condition, the topological number ν characterizing different topological phases can still be unambiguously extracted. As mentioned earlier, ν can be directly determined by the sign of the eigenenergy of $|\Phi\rangle$. Since $|\Phi\rangle$ is dominated by $|p, \leftarrow\rangle$ which is corresponding to $|7\rangle$, the eigenenergy of $|\Phi\rangle$ can be reliably obtained from $\{a_{4,m}\}$. The sign of the eigenenergy can be calculated as

$$\overline{sgn(E)} = \int_{-\infty}^{+\infty} sgn(E)p(E)dE = \int_{-\infty}^{+\infty} \frac{sgn(E)}{\sqrt{2\pi}\sigma} e^{-\frac{(E-E_c)^2}{2\sigma^2}} dE, \quad (5)$$

where E_c and σ are the fit center and the fit error of the energy spectrum (see Fig. 3d). Fig. 4b gives a clear representation of the topological phase transition by measuring ν versus μ , where a sharp change of ν occurs near $\mu \approx -1.3$. The deviation of the critical point from the theoretical expectation value $\mu = -1.29$ is due to the inaccuracy of measuring the very small eigenenergy (close to 0) near the critical point for which even a slight shift will change its sign. This deviation can be eliminated by using a NV sample with longer coherence time. Away from the critical point, the measured topological number will only have a negligibly small deviation from the exact value.

In conclusion, we have demonstrated quantum simulation of a topological phase transition with a single NV center at room temperature. Using quantum

algorithm of finding eigenvalues, we can not only obtain the dispersion relations, but also directly extract the topological number of the system. Different from the scheme of integration of dynamic responses¹¹⁻¹³, our approach of direct measurement of topological number can unambiguously give a discretized value of ν over almost all parameter space except for a small region around the phase transition. Even in the presence of large magnetical field fluctuations that may smear out the energy gap in the dispersion relations, the approach of direct extraction of topological number remains robust and unambiguously characterizes the topological phase transition.

We may further improve our NV-center-based quantum simulators by using isotopically purified diamond, with significantly extended electron spin coherence time²⁹. Moreover, with reliable control of multiple spins of the NV center³⁰, more complicated topological systems can be simulated. Utilizing entanglement can lead to a scalable quantum simulator of NV centers³¹. In addition, the quantum algorithm of finding eigenvalues can be extremely efficient for multiple spins, with only a polynomial time overhead with the number of spins³². Therefore, the NV-center-based quantum simulator is a very promising platform, which will provide a powerful tool to investigate novel quantum system.

Methods

Measurement of $a_{\psi,m}$. For the state:

$$\left(|6\rangle + \sum_{l=4,5,7,8} a_{l,m} |l\rangle \right) / \sqrt{2},$$

if we apply a $\pi/2$ manipulation between $|6\rangle$ and $|\psi\rangle$ along -x axis with phase θ , the state will be

$$\frac{1 - a_{\psi,m} e^{i\theta}}{2} |6\rangle + \frac{a_{\psi,m} + e^{-i\theta}}{2} |\psi\rangle + \sum_{l \neq \psi} a_{l,m} |l\rangle / \sqrt{2}.$$

The photoluminescence (PL) of this state is

$$\begin{aligned} PL(\theta) &= \left| \frac{1 - a_{\psi,m} e^{i\theta}}{2} \right|^2 PL_6 + \left| \frac{a_{\psi,m} + e^{-i\theta}}{2} \right|^2 PL_\psi + \sum_{l \neq \psi} \left| \frac{a_{l,m}}{\sqrt{2}} \right|^2 PL_l \\ &= \frac{1}{2} (PL_\psi - PL_6) (Re\{a_{\psi,m}\} \cos\theta + Im\{a_{\psi,m}\} \sin\theta) + C, \end{aligned} \quad (6)$$

where PL_l ($l = 4, 5, 6, 7, 8$) is the photoluminescence of pure states $|l\rangle$, C is a constant independent on θ . With different RF phases θ , a set of photoluminescence $PL(\theta)$ can be detected and fit with function $y(\theta) = y_0 + A \cos(\theta - \theta_0)$. Then $a_{\psi,m}$ can be obtained with:

$$a_{\psi,m} = \frac{2A \cos(\theta_0)}{PL_\psi - PL_6} + i \frac{2A \sin(\theta_0)}{PL_\psi - PL_6}. \quad (7)$$

In the case of $|\Psi\rangle = |5\rangle$, an additional π pulse between $|6\rangle$ and $|5\rangle$ is applied to make the oscillation amplitude more larger because $PL_4 > PL_5 \approx PL_6$.

1. Dirac, P. A. Quantised singularities in the electromagnetic field. In *Proceedings of the Royal Society of London A: Mathematical, Physical and Engineering Sciences*, vol. 133, 60–72 (The Royal Society, 1931). [2](#)
2. Dirac, P. The theory of magnetic poles. *Physical Review* **74**, 817 (1948). [2](#)
3. Thouless, D. J. Topological quantum numbers in nonrelativistic physics (1998). [2](#)
4. Klitzing, K. v., Dorda, G. & Pepper, M. New method for high-accuracy determination of the fine-structure constant based on quantized hall resistance. *Phys. Rev. Lett.* **45**, 494–497 (1980). [2](#)
5. Stormer, H. L., Tsui, D. C. & Gossard, A. C. The fractional quantum hall effect. *Rev. Mod. Phys.* **71**, S298–S305 (1999). [2](#)
6. Wen, X.-G. Topological orders in rigid states. *International Journal of Modern Physics B* **4**, 239–271 (1990). [2](#)
7. Qi, X.-L. & Zhang, S.-C. Topological insulators and superconductors. *Rev. Mod. Phys.* **83**, 1057–1110 (2011). [2](#)
8. Hasan, M. Z. & Kane, C. L. *Colloquium* : Topological insulators. *Rev. Mod. Phys.* **82**, 3045–3067 (2010). [2](#)

9. Alicea, J. New directions in the pursuit of majorana fermions in solid state systems. *Reports on Progress in Physics* **75**, 076501 (2012). [2](#), [3](#)
10. Beenakker, C. W. J. Random-matrix theory of majorana fermions and topological superconductors. *Rev. Mod. Phys.* **87**, 1037–1066 (2015). [2](#)
11. Gritsev, V. & Polkovnikov, A. Dynamical quantum hall effect in the parameter space. *Proceedings of the National Academy of Sciences* **109**, 6457–6462 (2012). [3](#), [12](#)
12. Schroer, M. D. *et al.* Measuring a topological transition in an artificial spin-1/2 system. *Phys. Rev. Lett.* **113**, 050402 (2014). [3](#), [12](#)
13. Roushan, P. *et al.* Observation of topological transitions in interacting quantum circuits. *Nature* **515**, 241–244 (2014). [3](#), [12](#)
14. Feynman, R. P. Simulating physics with computers. *International Journal of Theoretical Physics* **21** (1982). [3](#)
15. Lloyd, S. Universal quantum simulators. *Science* **273**, 1073–1078 (1996). [3](#)
16. Georgescu, I. M., Ashhab, S. & Nori, F. Quantum simulation. *Rev. Mod. Phys.* **86**, 153–185 (2014). [3](#)

17. Gruber, A. *et al.* Scanning confocal optical microscopy and magnetic resonance on single defect centers. *Science* **276**, 2012–2014 (1997). [3](#)
18. Maurer, P. C. *et al.* Room-temperature quantum bit memory exceeding one second. *Science* **336**, 1283–1286 (2012). [3](#)
19. Ju, C. *et al.* NV-center-based digital quantum simulation of a quantum phase transition in topological insulators. *Phys. Rev. B* **89**, 045432 (2014). [3](#)
20. Abrams, D. & Lloyd, S. Quantum algorithm providing exponential speed increase for finding eigenvalues and eigenvectors. *Phys. Rev. Lett.* **83**, 5162–5165 (1999). [3](#), [6](#), [8](#)
21. Oreg, Y., Refael, G. & von Oppen, F. Helical liquids and majorana bound states in quantum wires. *Phys. Rev. Lett.* **105**, 177002 (2010). [3](#)
22. Lutchyn, R. M., Sau, J. D. & Das Sarma, S. Majorana fermions and topological phase transition in semiconductor or superconductor heterostructures. *Phys. Rev. Lett.* **105**, 077001 (2010). [3](#)
23. Jiang, L. *et al.* Magneto-josephson effects in junctions with majorana bound states. *Phys. Rev. B* **87**, 075438 (2013). [3](#)

24. Alicea, J., Oreg, Y., Refael, G., von Oppen, F. & Fisher, M. P. A. Non-abelian statistics and topological quantum information processing in 1d wire networks. *Nature Phys.* **7**, 412–417 (2011). [3](#)
25. Kitaev, A. Y. Unpaired majorana fermions in quantum wires. *Physics-Uspekhi* **44**, 131 (2001). [5](#)
26. Loubser, J. H. N. & Wyk, J. A. v. Electron spin resonance in the study of diamond. *Rep. Prog. Phys.* **41**, 1201 (1978). [6](#)
27. Shi, F. *et al.* Sensing and atomic-scale structure analysis of single nuclear-spin clusters in diamond. *Nature Phys.* **10**, 21–25 (2014). [9](#)
28. Jacques, V. *et al.* Dynamic polarization of single nuclear spins by optical pumping of nitrogen-vacancy color centers in diamond at room temperature. *Phys. Rev. Lett.* **102**, 057403 (2009). [9](#)
29. Balasubramanian, G. *et al.* Ultralong spin coherence time in isotopically engineered diamond. *Nature Materials* **8**, 383–387 (2009). [10](#), [12](#)
30. Bonato, C. *et al.* Optimized quantum sensing with a single electron spin using real-time adaptive measurements. *Nat. Nanotechnol.* **advance online publication** (2015). [12](#)

31. Yao, N. Y. *et al.* Scalable architecture for a room temperature solid-state quantum information processor. *Nature Commun.* **3**, 800 (2012). [12](#)
32. Abrams, D. S. & Lloyd, S. Quantum algorithm providing exponential speed increase for finding eigenvalues and eigenvectors. *Phys. Rev. Lett.* **83**, 5162–5165 (1999). [12](#)

Acknowledgements This work was supported by the National Key Basic Research Program of China (Grant No. 2013CB921800), the National Natural Science Foundation of China (Grant Nos. 11227901, 91021005, 11104262, 31470835), and the Strategic Priority Research Program (B) of the CAS (Grant No. XDB01030400). LJ acknowledges the support from ARL-CDQI, ARO (Grant Nos. W911NF-14-1-0011, W911NF-14-1-0563), AFOSR MURI (Grant Nos. FA9550-14-1-0052, FA9550-14-1-0015), Alfred P. Sloan Foundation (Grant No. BR2013-049), the Packard Foundation (Grant No. 2013-39273).

Author contributions J.D. and L.J. proposed the idea. C.J. and Y.L. designed the experimental proposal. F.K., X.K. and P.W. prepared the experimental set-up. M.W. prepared the diamond sample. F.K. and Y.L. performed the experiments. J.D. supervised the setup and experiments. C.J., F.K. and C.L. carried out the calculation. L.J., C.L., C.J., and F.K. wrote the paper. All authors analysed the data, discussed the results and commented on the manuscript.

Competing Interests The authors declare that they have no competing financial interests.

Correspondence Correspondence and requests for materials should be addressed to Liang Jiang and Jiangfeng Du (email: liang.jiang@yale.edu; djf@ustc.edu.cn).

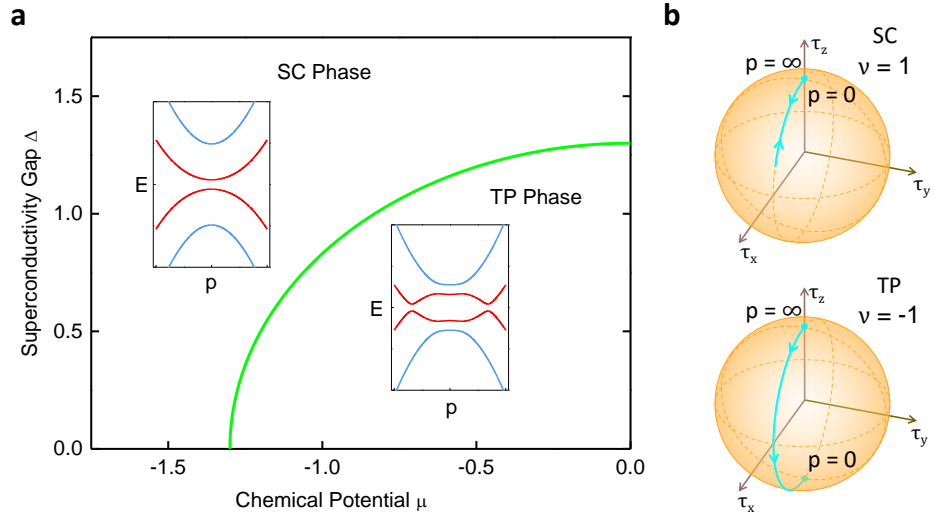


Figure 1: **Phase diagram and geometric illustration of the topologically distinct phases.** **a**, Phase diagram of quantum wire system (calculated at $B_x = 1.3$). The green line gives the boundary between SC phase and TP phase. The energy dispersion relations of an SC point and a TP point are plotted in the insets. **b**, Geometric illustration of topological difference between the SC and the TP phases.

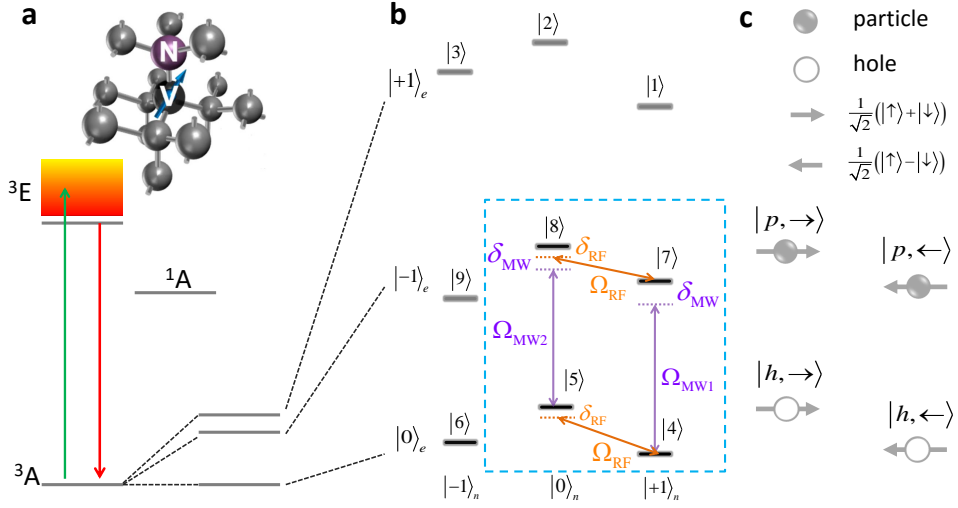


Figure 2: **NV system and its correlation with QW system.** **a**, Structure and energy levels of the NV centers. **b**, Hyperfine structure of the coupling system with NV electron spin and ^{14}N nuclear spin. The 9 energy levels are labeled as $|1\rangle$ to $|9\rangle$. The quantum simulation is carried out in the subspace spanned by $\{|4\rangle, |5\rangle, |7\rangle, |8\rangle\}$. Two MW pulses (purple arrows) and two RF pulses (orange arrows) are applied simultaneously to selectively drive the corresponding electron and nuclear spin transitions. **c**, Four basis states of QW system corresponding to the four NV states inside the square box.

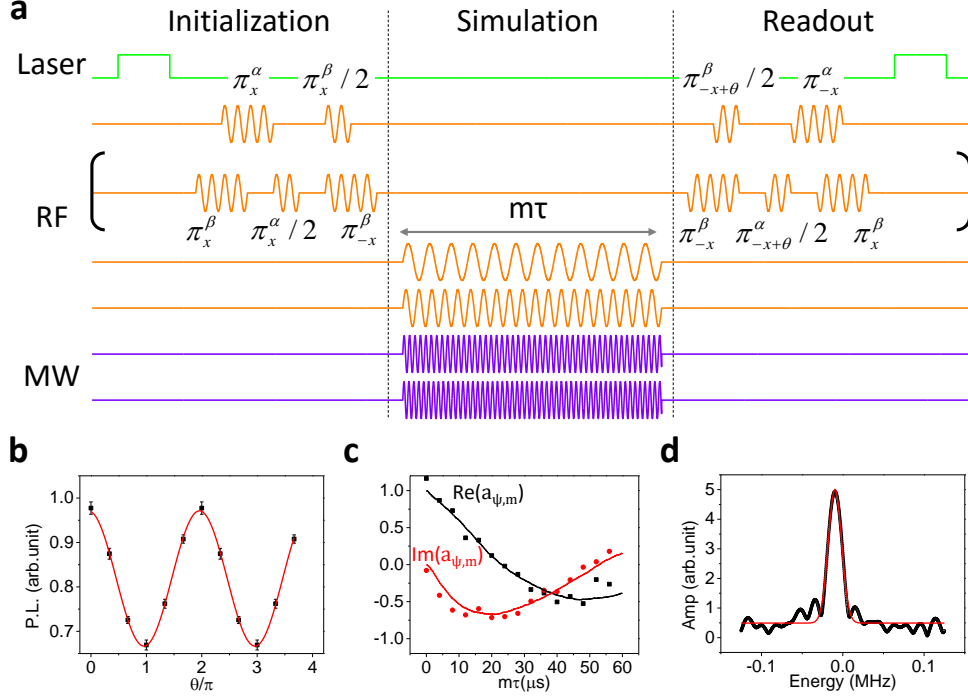


Figure 3: Simulation QW Hamiltonian and detection its eigenvalues. **a**, The pulse scheme. The superscript α (β) of the RF pulses indicates the nuclear spin operation between $|4\rangle$ and $|5\rangle$ ($|5\rangle$ and $|6\rangle$). For the initialization and readout parts there are two pulse sequences, which corresponds to the two initial state cases $|\Psi\rangle = |5\rangle$ (the upper pulse sequence) and $|4\rangle$ (the lower bracketed pulse sequence), respectively. **b**, Photoluminescence changes versus different RF $\pi/2$ pulse phase θ for fixed evolution time $m\tau$. The points are the experimental data and the curve is the sine function fit. Error bars indicate ± 1 s.d. induced by the photon shot noise. **c**, Measurement of $a_{\psi,m}$ with different evolution time $m\tau$. Black and red lines are the numerical calculation results. **d**, The energy spectrum of the simulated Hamiltonian yielded from the Fourier transform of the time-domain data in **c**. A Gauss function fit (the curve) is performed to get the exact eigenenergy value.

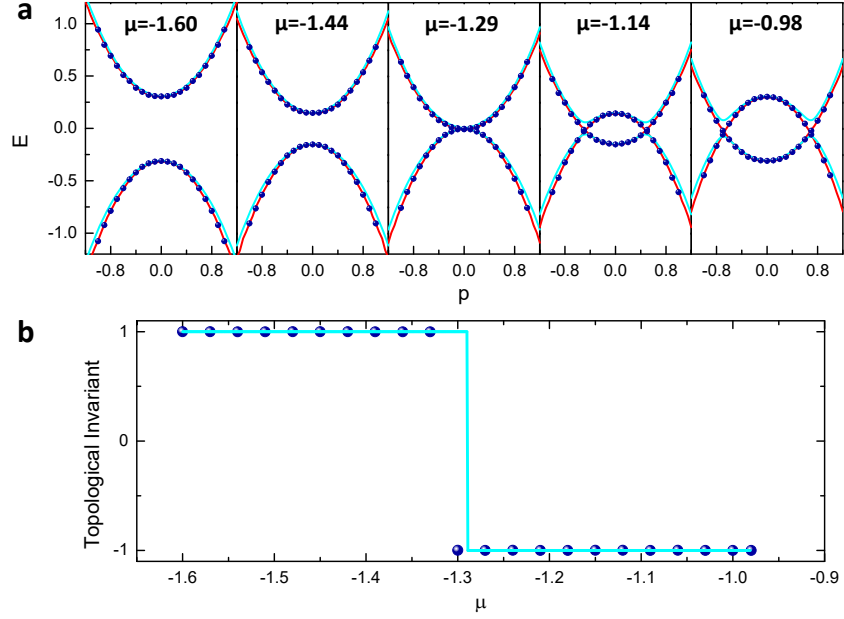


Figure 4: **Energy dispersion relations and topological phase transition.** **a**, Energy dispersion relations with different chemical potential μ . The points, light cyan lines, and red lines represent the experimental, analytical, and numerical results, respectively. Error bars given by fit error are smaller than the symbols. As the energy bands are symmetrical about $p = 0$, only the right half points (i.e. $p \geq 0$) are actually measured in the experiment. **b**, The measured topological number ν versus the chemical potential μ , which shows a topological phase transition happened near $\mu \approx -1.3$. The cyan line is the theoretical prediction.